Effect of Surface Roughness Geometry on Boundary-Layer Transition and Far-Field Noise

Ye, Q.; Avallone, F.; Ragni, D.; Choudhari, Meelan; Casalino, D.

DOI
10.2514/1.J059335

Publication date
2021

Document Version
Final published version

Published in
AIAA Journal: devoted to aerospace research and development

AIAA JOURNAL
Vol. 59, No. 7, July 2021

Effect of Surface Roughness Geometry on Boundary-Layer Transition and Far-Field Noise

Qingqing Ye,* Francesco Avallone,† and Daniele Ragni†
Delft University of Technology, 2629HS Delft, The Netherlands
Meelan Choudhari‡
NASA Langley Research Center, Hampton, Virginia 23681
and
Damiano Casalino§
Delft University of Technology, 2629HS Delft, The Netherlands

https://doi.org/10.2514/1.J059335

Surface roughness elements are often used to force laminar to turbulent transition in aerodynamic and aeroacoustic wind-tunnel experiments. The statistical features and spectral content of the pressure fluctuations in the resulting turbulent boundary layer at the trailing edge can affect far-field noise. To elucidate this dependence, boundary-layer transition induced by randomly distributed roughness elements and a zigzag strip of the same height over a NACA 0012 airfoil is investigated experimentally. The effects of roughness geometry on the near-field flow topology, transition location, and far-field noise are addressed in the common experimental setting for the first time. For a fixed roughness height, distributed roughness elements are less effective in forcing transition than the zigzag strip at low freestream velocity ($u_\infty < 20$ m/s). As u_∞ increases, the transition front for the distributed roughness elements moves closer to the roughness location, reaching the same or even further upstream locations compared to the transition onset in the presence of the zigzag strip. The far-field noise depends on the transition location. For $u_\infty \leq 20$ m/s, a higher noise level is measured for the distributed roughness elements with respect to the zigzag strip. In contrast, for $u_\infty > 20$ m/s, the earlier onset of transition with the distributed surface roughness leads to a lower noise level than that with the zigzag strip. The data confirm that an adequate characterization of the boundary-layer transition is necessary when measuring the far-field noise during wind-tunnel experiments.

Nomenclature

b	=	span of the airfoil model, mm
BANC	=	Benchmark Problems for Airframe Noise Computations
c	=	chord of the airfoil model, mm
c_0	=	speed of sound, m/s
D	=	diameter of the microphone array, m
dbA	=	A-weighted decibel
f	=	frequency, Hz
H	=	shape factor
L_p	=	1/3-octave band sound pressure level (reference sound pressure 20 μPa), dB
M_∞	=	freestream Mach number
R	=	reference observer distance, m
Re_c	=	chord-based Reynolds number
St	=	Strouhal number
t	=	recording time, s
u_e	=	boundary-layer edge velocity, m/s
u_τ	=	friction velocity, m/s
u_∞	=	freestream velocity, m/s
u'	=	velocity fluctuations, m/s
x	=	Cartesian coordinate axes aligned with the airfoil chord
x_t	=	chordwise location of transition front
y	=	Cartesian coordinate axes normal to airfoil chord and span
z	=	Cartesian coordinate axes aligned with the airfoil span
γ	=	intermittency factor
Δ	=	value difference
δ_{99}	=	boundary-layer thickness, mm
δ^*	=	boundary-layer displacement thickness, mm
θ	=	boundary-layer momentum thickness, mm
ν	=	kinematic viscosity, m^2/s
$\langle\rangle$	=	root mean square

I. Introduction

AERODYNAMIC noise generated by the convection of a turbulent boundary layer past a sharp trailing edge of an airfoil is a relevant noise source for wind turbines [1] and aircraft [2–4]. The intensity of far-field noise and its spectral distribution strongly depends on the boundary-layer properties at the trailing edge [5,6], which is affected by the location of transition onset. Uncertainty in the transition location has an effect on the comparison between experiments carried out in different wind tunnels, which may differ in the intensity of freestream turbulence and in the way the process of laminar to turbulent transition is induced in the boundary-layer flow [7,8]. Herr et al. [9] and Herr and Kamruzzaman [10] provided a comprehensive comparison of numerical simulations and wind-tunnel measurements of trailing-edge noise for both symmetric and cambered airfoils within the framework of the BANC series of workshops hosted by the AIAA [11], indicating the disparity on the far-field noise level of approximately ± 3 dB between experimental results even when obtained with the same setup and nominal flow conditions.

Surface roughness elements are conventionally used as devices to force laminar to turbulent transition in controlled wind-tunnel experiments. Roughness elements are typically divided into two main categories: two-dimensional roughness elements (e.g., wires, steps, and gaps), and three-dimensional isolated or distributed roughness

Presented as Paper 2019-2551 at the 25th AIAA/CEAS Aeroacoustics Conference, Delft, The Netherlands, May 20–23, 2019; received 17 December 2019; revision received 23 November 2020; accepted for publication 7 December 2020; published online 24 February 2021.

*Postdoctoral Researcher, Department of Aerodynamic, Wind Energy and Propulsion; q.ye-1@tudelft.nl.
†Assistant Professor, Department of Aerodynamic, Wind Energy and Propulsion. Member AIAA.
‡Aerospace Technologist. Fellow AIAA.
§Full Professor, Department of Aerodynamic, Wind Energy and Propulsion. Member AIAA.

elements. Two-dimensional roughness elements affect the transition process via enhancing the amplification of Tollmien–Schlichting (TS) waves, especially within the separation and recovery regions behind the roughness elements [12]. An increase of the Reynolds number leads to the growth of the TS wave amplitude [13], resulting in a gradual upstream shift of the transition location toward the location of the roughness element [14]. Three-dimensional roughness elements induce a localized spanwise deflection of the boundary-layer flow. Counterrotating streamwise vortex pairs are generated in the wake of roughness elements [15–17], resulting in the formation of low- and high-speed streaks, which modulate the surface shear along the spanwise direction. Once the streak amplitude exceeds a critical value, the streak will be subject to a secondary instability in the form of either sinuous or varicose modulation that eventually leads to breakdown to turbulence [18].

Compared with isolated roughness elements, distributed roughness elements are more widely used as a tripping device in wind-tunnel experiments due to their effectiveness in promoting transition and improved spanwise uniformity of the downstream turbulent flow [6,19–21]. In reality, wind-turbine blades also suffer from erosion caused by sand or hail, insect deposits, and icing, resulting in the formation of similar rough surfaces close to the leading edge [22]. To avoid the sensitivity of airfoil self-noise to the transition location during wind-tunnel experiments at low Reynolds numbers, oversized boundary-layer trips are often used. Despite ensuring a fully turbulent boundary layer at the trailing edge [23], the large-sized boundary-layer trips may introduce coherent flow structures that persist up until the trailing edge, thus altering the streamwise and spanwise correlations of the turbulent boundary layer and affecting trailing-edge noise [20]. Therefore, a good knowledge and control of the transition location is necessary to accurately predict far-field noise.

Acoustic measurements with microphone arrays have been used in recent years to investigate the effect of surface roughness on the trailing-edge noise. Hutcheson and Brooks [20] measured trailing-edge noise from a NACA 63-215 airfoil, where the boundary layer was tripped with steel grits and serrated tape of 0.29 mm height over the first 5% of the chord. It was found that the trailing-edge noise is the dominant noise source in the low-frequency range. On the other hand, the noise source due to surface roughness close to the leading edge becomes the dominant contributor at the higher frequencies ($f > 12.5$ kHz). Cheng et al. [21] investigated the effect of roughness induced by surface icing on the broadband noise of rotors. They found that the height of surface roughness changes both the boundary-layer thickness and the turbulent intensity at the trailing edge. In turn, the increase in the turbulent intensity leads to a significant trailing-edge noise increase at the frequencies higher than 4 kHz. For a full-scale three-blade wind turbine, Oerlemans et al. [1] performed acoustic measurements to detect the dominant noise sources. When the blade was equipped with relatively larger-sized roughness elements with respect to the one needed to promote transition, the overall sound level was found to increase by about 3.6 dB A compared with clean turbine blade conditions. The noise source extent also increases when the frequency is lower than 2 kHz.

Until recently, the research on the effect of distributed surface roughness on boundary-layer transition did not devote enough attention to identify the correlation between the flow topology, the underlying transition mechanism, and the far-field noise. Winkler et al. [24] studied the effect of step and serration trip over a NACA 6512-63 airfoil on trailing-edge noise using a large-eddy simulation. Transition onset location is strongly influenced by the roughness geometry, leading to different flow structures at the trailing edge and in the airfoil wake. The far-field noise prediction indicates that the noise level for the step is around 10 dB higher than that for serrated trip. The recent study by Ribeiro et al. [25] provided the first set of numerical simulations to address the effects of sand-grain surface roughness on trailing-edge noise over a NACA 0012 airfoil. They found that with the surface roughness being placed over the leading edge, the far-field noise level is 10 dB lower in relation to that of the clean airfoil configuration. The present research aims at extending the current understanding on these aspects via a deeper characterization of the flowfield. For this purpose, measurements were carried out in an experimental setup similar to that of Brooks et al. [6] on airfoil trailing-edge noise. Randomly distributed roughness elements were placed on a NACA 0012 airfoil at a 0 deg angle of attack. Since zigzag strips are also widely used as three-dimensional boundary-layer tripping devices [26,27], a zigzag strip with the same height and streamwise length as the distributed roughness patch was tested for comparison. The distribution of the roughness elements was measured via a three-dimensional laser scanner, providing a reference geometry for future numerical study. Infrared thermography was used to measure the surface temperature, enabling the detection of the transition location. The flow topology around and downstream of the roughness elements was characterized by the time-averaged velocity field measured via hot-wire anemometry. The turbulent behavior was elaborated by the turbulent intermittency and power spectral density in the frequency domain. The noise sources were detected and quantified by using phased microphone array measurements to highlight the influence of different roughness geometries on the far-field noise.

II. Experimental Setup and Measurement Techniques

A. Flow Conditions and Test Facilities

Experiments were performed in the anechoic vertical open-jet wind tunnel of the Aerodynamics Laboratories of the Aerospace Engineering Faculty at Delft University of Technology. The wind-tunnel test section is 0.4×0.7 m^2, which follows a contraction ratio of 15:1. The maximum operating velocity with this section is 42.5 m/s. The turbulence intensity at this velocity is below 0.1%. The freestream velocity distribution across the test section has a uniformity of 0.5%.

A NACA 0012 airfoil with a 300 mm chord c and 400 mm span b was installed between side plates in the symmetry plane of the test section. The airfoil was set at a 0 deg angle of attack. A Cartesian system of coordinate axes centered at the leading edge of the airfoil is introduced such that the x axis is aligned with the airfoil chord, the z axis is oriented along the span, and the y axis is normal to both of them to form a right-handed reference system. The conceptual sketch of the model arrangement is shown in Fig. 1. The alignment of the airfoil is checked by 24 Honeywell TruStability pressure sensors. Twelve pressure sensors are distributed along each side of the airfoil in the chordwise range of $x/c = [0.30, 0.70]$. The pressure sensors are aligned with an angle of 22 deg with respect to the chord to avoid flow interference between neighboring sensors. The data acquisition is performed at 2000 Hz for 60 s. The pressure coefficient difference Δc_p between two sides of airfoil at different freestream velocities is calculated and compared with the predicted data by XFOIL [28] to determine the angle of attack. As shown in Fig. 2, the angle of attack falls around 0.15 ± 0.1 deg.

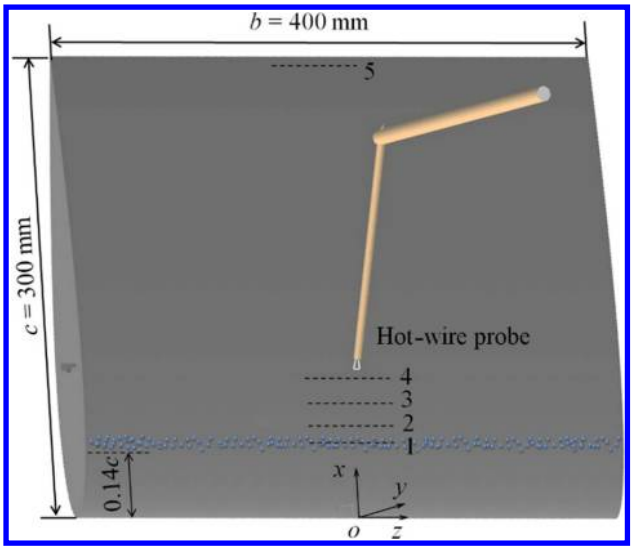

Fig. 1 Sketch of the experimental configuration. Measurement planes of hot-wire anemometry shown by dashed lines 1–5, corresponding to locations of $x/c = 0.16$, 0.19, 0.24, 0.29, and 0.95, respectively.

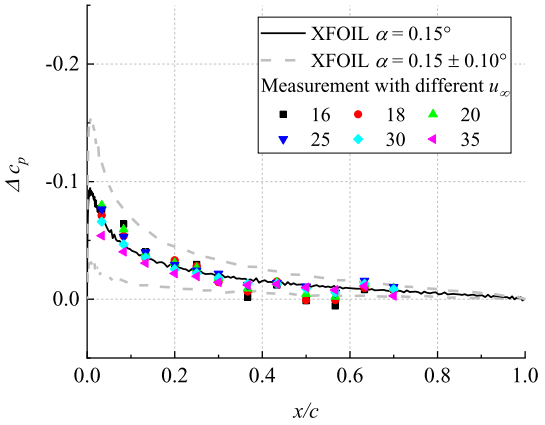

Fig. 2 Pressure coefficient difference distribution Δc_p at different flow conditions.

Two boundary-layer tripping devices were tested: randomly distributed roughness elements, and a zigzag strip. The roughness elements were installed over the chordwise range of $x/c = [0.14, 0.18]$ on both suction and pressure sides of the airfoil over the entire span. The distributed roughness elements have spherical shapes (referred to as grit) with a nominal diameter of 0.3 ± 0.1 mm. The density of the roughness elements is approximately two elements per millimeter. The roughness distribution was measured with a high-speed laser scanner (Micro-Epsilon scanCONTROL 2925, with maximum frequency of 2 kHz). It is a compact device that produces laser sheets and receives the reflected laser light from the target surface using a built-in optical system. The working principle of the scanner follows the laser line triangulation. The laser sheet produced by the scanner intersects the top half of the spherical grit elements. As a result, the roughness elements are identified with a hemispherical shape. The laser sheet with a length of 29 mm was aligned in the streamwise direction x, with 1280 points captured in a single streamwise profile. The distance from the airfoil surface to the scanner is 65 ± 1 mm, which falls in the focus range of the scanner. The spanwise surface variation was measured by moving the scanner with an in-house traverse control system with a step size of 0.025 mm in the range $z/c = [-0.08, 0.08]$. The scanning resolutions along the x, y, and z directions are 22, 2, and 25 μm, respectively. The scanned surfaces on the upper and lower surfaces are shown in Fig. 3. For comparison, a conventional zigzag strip with the same height of 0.3 mm and streamwise extent of $0.04c$ was selected. The top angle of the zigzag strip is 60 deg.

Experiments were performed at six freestream velocities ($u_\infty = 16, 18, 20, 25, 30,$ and 35 m/s). The corresponding chord-based Reynolds number ($Re_c = u_\infty c/\nu$) varies from 3.29×10^5 to 7.20×10^5. The detailed test conditions (Re_c and Mach number M_∞) are summarized in Table 1.

B. Infrared Thermography

Infrared (IR) thermography measurements were carried out with an Optris PI640 IR system. The camera has a focal-plane array detector with a sensitivity of 75 mK. The sensor size of the camera is 640×480 pixels. The spectral response of the sensor falls in the range of 7.5–13 μm. An objective with a focal length of 41.5 mm was mounted on the IR camera. The recording rate was 30 Hz at full resolution. The measurement domain captured the full airfoil chord. The resultant spatial resolution is 2.19 pixels/mm. The camera was mounted at an angle of approximately 20 deg with respect to the symmetry plane of the tunnel to avoid self-reflection. To increase the temperature difference with the flow, the surface of the model was heated with two 1 W halogen lamps. The IR camera was shielded with an aluminum foil to avoid heat radiation from the lamp. Because the measured surface temperature distributions are used to extract the transition location, no further corrections are applied to the emissivity and the reflectivity. The surface temperature nonuniformity due to preheating was corrected by subtracting the surface temperature measured without flow.

Table 1 Test conditions

	u_∞, m/s					
	16	18	20	25	30	35
Re_c	3.29×10^5	3.70×10^5	4.11×10^5	5.14×10^5	6.17×10^5	7.20×10^5
M_∞	0.047	0.053	0.058	0.073	0.088	0.102

C. Hot-Wire Anemometry

Hot-wire anemometry measurements were carried out to capture the velocity field behind the roughness elements (Fig. 1). A 5-μm-diameter single-wire probe (Dantec Dynamics P11) was used in conjunction with a constant-temperature bridge (TSI IFA-300). The development of the flowfield was measured in y–z cross planes at four streamwise positions ($x/c = [0.16, 0.19, 0.24, 0.29]$), including both directly above the middle of the roughness strip and their near wake (see Fig. 1). The spanwise extents of the measurement planes are $z/c = [-0.08, 0.08]$ and $[-0.08, 0.00]$ for randomly distributed roughness elements and the zigzag strip, respectively. For the zigzag strip, the measurement planes extended across four spanwise wavelengths. The trailing-edge boundary-layer properties were measured at $x/c = 0.95$ over a spanwise range of $z/c = [-0.08, 0.00]$. The wall-normal depth of each measurement plane is adapted to fully capture the boundary-layer thickness and to account for the change in the wall location at different streamwise positions. Thirty points were measured in each boundary-layer profile. The movement of the hot-wire probe was controlled by an in-house traverse system with 3 deg of freedom, yielding an accuracy of 13 μm in all three directions. The spanwise step size is 1 mm ($0.003c$). The wall-normal spacing varies from point to point, depending on the local velocity gradient. The minimum wall-normal step is 0.02 mm at the closest distances from the wall of 0.18 and 0.27 mm for the freestream velocities of 20 and 25 m/s, respectively. The measurement data were acquired at a sampling frequency of 50 kHz. A low-pass filter was applied with a cutoff frequency of 20 kHz. A measurement duration of 2 s was used for each point, ensuring good statistical convergence of the targeted flow statistics. The hot-wire calibrations were performed in the wind tunnel close to the nozzle exit against a pitot-static tube. The flow

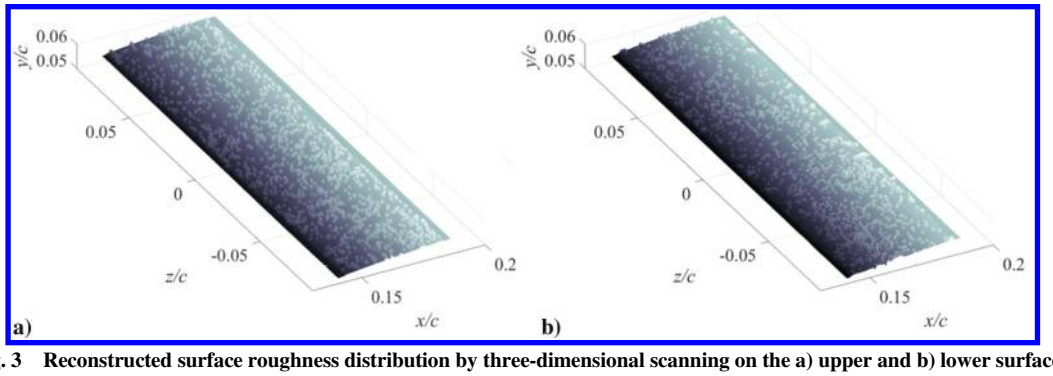

Fig. 3 Reconstructed surface roughness distribution by three-dimensional scanning on the a) upper and b) lower surfaces.

temperature and atmospheric pressure were corrected to compensate for change of conditions.

The uncertainty on normalized mean velocity is estimated from the following expression [29]:

$$\varepsilon_u = \frac{\sigma_u}{\sqrt{N}} \tag{1}$$

where σ_u is the measured typical intensity of velocity fluctuations ($\langle u' \rangle / u_\infty$) of approximately 0.09, and N is the ensemble size of 100,000 for the present experiment. The uncertainty level of the mean velocity is 0.028%.

The uncertainty of the root mean square (RMS) of normalized velocity fluctuations is estimated using the following expression:

$$\varepsilon_{\langle u' \rangle} = \frac{\sigma_u}{\sqrt{2(N-1)}} \tag{2}$$

yielding the level of approximately 0.020%.

D. Acoustics Measurement

The location and amplitude of the acoustic sources were measured using a phased microphone array with 64 G.R.A.S. 40PH free-field microphones (frequency response: ±1 dB, frequency range: 10 Hz to 20 kHz, and maximum output: 135 dB at reference sound pressure 2×10^{-5} Pa). The microphones are equipped with constant current power (CCP) preamplifiers to measure far-field noise from the airfoil trailing edge with transition induced by both the distributed roughness elements and the zigzag strip. The microphone array is parallel to the chord centerplane of the model at a 0 deg angle of attack, with a distance R of 1.30 m between the two planes. The microphone placement follows an optimized array distribution with nine spiral arms and seven microphones along each arm [30], as shown in Fig. 4a. Close to the center of the array, an extra microphone is added, located at $(x, y, z) = (0.1, 1.3, 0)$. The microphone array has an effective extent of 2 m in the streamwise direction and 1 m in the spanwise direction. Compared with the Underbrink design [31], the optimized array distribution reduces the main lobe width and maximum side lobe level of the noise source.

Measurements were recorded at a sampling frequency of 50 kHz for 60 s. The acoustic data were processed with a Fourier transform using a window size of 5000 samples ($\Delta t = 100$ ms). A Hanning-weighting function with 50% overlap was used, resulting in a frequency resolution of $\Delta f = 10$ Hz. The signal-to-noise ratio of the measurement is calculated by subtracting the background noise of the tunnel without the model from the corresponding noise level with the installed model. The noise spectrum is obtained by the center microphone in the array, yielding a range of 4–10 dB across a frequency range of 800 to 4000 Hz for all the cases, as shown in Fig. 5, in alignment with previous experiments with similar setups [32].

Conventional frequency domain beamforming (CFDBF) [33] was performed on a grid in the ranges of $x/c = [-3.00, 3.67]$ and $z/c = [-1.67, 1.67]$. The grid point resolution is 10 mm. A source power integration technique [34] was used, assuming the presence of a line noise source located at the airfoil trailing edge. Results were integrated in the ranges of $x/c = [0.90, 1.10]$ and $z/c = [-0.50, 0.50]$. To avoid side lobe contributions, the integration area is limited to 6 dB below the peak level of the noise source. The sound intensity per unit span obtained using various spanwise extents of integration region is nearly uniform. According to the Rayleigh criterion [35], the minimum distance for which the microphone array can distinguish two noise sources is $R_c = R \tan(1.22 c_0 / fD)$, where D is the diameter of the microphone array and c_0 is the speed of sound. For the highest frequency of interest equal to 4000 Hz, the minimum distance R_c equals 67 mm. As a result,

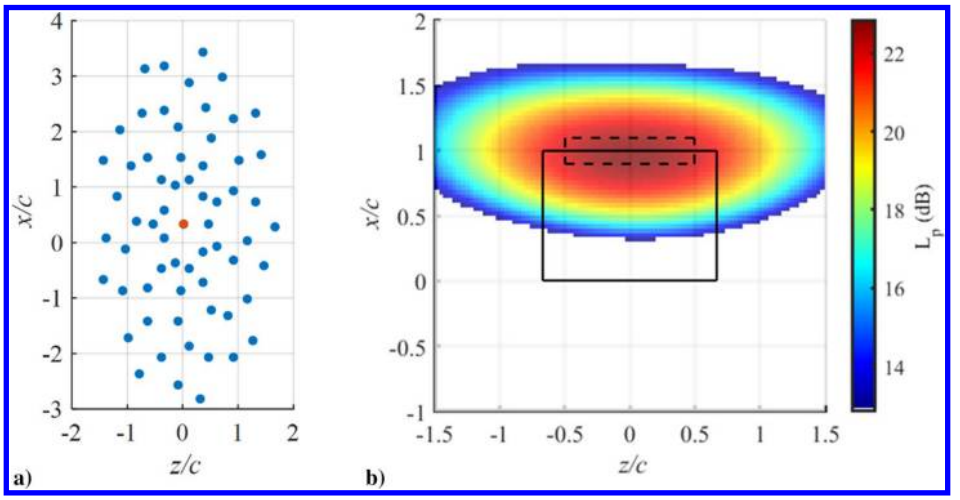

Fig. 4 Distribution of microphone array (Fig. 4a) and source map in x–z plane (Fig. 4b) for 1/3-octave band with center frequency of 1250 Hz and $u_\infty = 25$ m/s. Solid and dashed boxes indicate the airfoil model and the integration area, respectively.

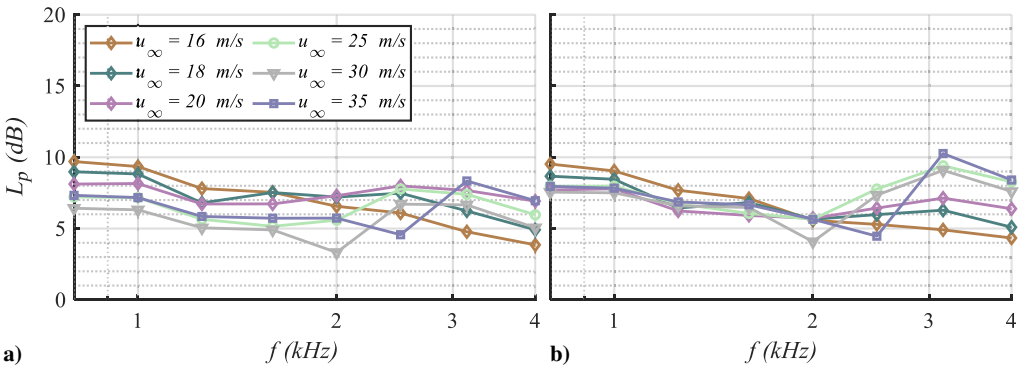

Fig. 5 Signal-to-noise ratio for the averaged array signal for a) grit and b) zigzag.

the grid spacing is seven times smaller than R_c. The uncertainty of sound power estimated by the CFDBF method is less than 1 dB [36]. Compared with averaged results from all the microphones within the array, the noise level estimated by the CFDBF shows a difference of 3 dB [34]. One example of the source map at 1250 Hz for the freestream velocity of 25 m/s is shown in Fig. 4b. The noise source is detected at the trailing edge with satisfactory resolution, similar to previous experimental results [6,37]. In fact, when checking the noise source map for both boundary-layer trips across all flow conditions in the frequency range of interest, only trailing-edge noise is observed in the source maps. No leading-edge noise source appears, indicating that the vortical structures in the vicinity of the boundary-layer trips do not play a role in the noise generation in the present experiment. The noise level is integrated in the dashed box area at the trailing edge to further eliminate the leading-edge effect.

III. Surface Temperature Distribution and Transition Location Detection

The development of the flowfield over the suction side of the airfoil is first described through the surface temperature distributions shown in Fig. 6. The effects of the grit and the zigzag strip at six different freestream velocities ($u_\infty = 16, 18, 20, 25, 30$, and 35 m/s, respectively) on boundary-layer transition are compared. The onset of transition is detected from the decrease in surface temperature caused by the higher convective heat transfer downstream of this location. The transition locations for all flow conditions are reported in Table 2, which is obtained by averaging the location over the span to account for the nonuniform distribution of transition front. The streamwise ranges of transition onset locations are also included.

When $u_\infty \leq 20$ m/s, the grit is less effective in promoting transition in comparison to the zigzag strip of the same height. At $u_\infty = 16$ m/s, the transition front is at $x_t/c = 0.70$ for the grit (Fig. 6a) and is uniform in the spanwise direction. No evident footprint of flow structures in the near wake of the roughness elements is detected, indicating a relatively lower amplitude of the velocity streaks. Compared with the undisturbed boundary layer for the same freestream velocity, the transition front moves upstream from $x_t/c = 0.84$ to 0.70 (see Table 2). For the zigzag strip, low-temperature regions appear directly downstream of the front facing apexes of the zigzag (Fig. 6b). The intensity of the low-temperature regions decreases farther downstream until the transition onset (occurring at $x_t/c = 0.68$), which is slightly upstream of the transition location for the randomly distributed roughness elements.

Increasing u_∞ to 18 m/s, the transition front moves slightly upstream to $x_t/c = 0.57$ for the grit and all the way to $x_t/c = 0.28$ for the zigzag strip (Figs. 6c and 6d, respectively). Due to the nonuniform distribution of the grit, two turbulent wedges originate as far upstream as $x_t/c = 0.25$ near $z/c = 0.28$ and $z/c = -0.18$, respectively. From a direct visual inspection, the grit appears more densely distributed near these two locations. For the zigzag, additional low-temperature regions with stronger intensity are formed at the transition front. The spanwise locations of the new structures correspond to downstream-pointing apexes of the zigzag. At $u_\infty = 20$ m/s, the transition front moves to $x_t/c = 0.42$ and 0.23 for grit and zigzag, respectively (Figs. 6e and 6f). Although the turbulent wedges occur most upstream at $x_t/c = 0.23$ in a jagged pattern, a better spanwise uniformity of the transition front is provided by the zigzag strip.

For u_∞ equal to 25 and 30 m/s (Figs. 6g and 6h and 6i and 6j, respectively), the transition front moves closer to the roughness elements, yielding comparable tripping effectiveness at this flow condition with good spanwise uniformity. At the highest u_∞ of 35 m/s (Figs. 6k and 6l), transition occurs over the roughness strip for the grit, due to the sensitivity of the flow to the upstream elements of the roughness strip. Conversely, for the zigzag strip, the transition front is located at $x_t/c = 0.19$, which is directly downstream of the zigzag strip. In this case, the disturbances are produced on the shear layer originating from the zigzag, as proposed by Elsinga and Westerweel [38]. These disturbances are amplified as the shear layer develops downstream. Transition onset is expected to occur when the fluctuation level reaches the critical value [39].

IV. Near Wake of Roughness Elements

A. Flow Topology

To further investigate the flow topology in the vicinity of the roughness elements and within their wake, the time-averaged velocity fields are measured via hot-wire anemometry at two freestream velocities of $u_\infty = 20$ and 25 m/s, respectively. The modification of the mean flowfield and production of turbulent fluctuations by both roughness elements are inspected by the cross-plane contours of the root mean square of the velocity fluctuations ($\langle u' \rangle / u_e$) at four streamwise positions ($x/c = [0.16, 0.19, 0.24, 0.29]$), as shown for both types of trips in Fig. 7 for $u_\infty = 20$ m/s and in Fig. 8 for $u_\infty = 25$ m/s. The contour lines of time-averaged velocity (u/u_e) are superimposed to support the interpretation.

For $u_\infty = 20$ m/s, an undulated shear flow develops above both roughness configurations at $x/c = 0.16$ (Figs. 7a and 6b, respectively). The distribution of velocity fluctuations is uniform along the spanwise direction. The maximum intensity of velocity fluctuations produced by the grit is approximately $0.04u_e$, which is nearly half as large as the peak velocity fluctuations in the wake of the zigzag.

At $x/c = 0.19$ (Fig. 7c; i.e., slightly downstream of the roughness strip), the undulated shear layer induced by the grit remains uniformly distributed in the spanwise direction, showing no increase of the velocity fluctuation intensity relative to $x/c = 0.16$. At $x/c = 0.24$ (Fig. 7e), a low-speed region of narrow spanwise extent is formed at $z/c = -5.33 \times 10^{-2}$. The inflectional instability at the wall-normal shear layer of the former region induces peak velocity fluctuations. Further downstream, at $x/c = 0.29$ (Fig. 7g), this low-speed region expands in the spanwise direction, inducing two additional low-speed regions in its vicinity ($z/c = -6.00 \times 10^{-2}$ and -4.67×10^{-2}). The intensity of the velocity fluctuations further increases, reaching a maximum of $0.1u_e$. Two additional locations with secondary local peaks of the velocity fluctuations can be observed at $z/c = -1.00 \times 10^{-2}$ and 8.00×10^{-2}. As found in the surface temperature distribution in Fig. 6e, these locations correspond to the inception of turbulent wedges.

For the zigzag strip, spanwise periodic low- and high-speed regions start to emerge at $x/c = 0.19$ (Fig. 7d). The locations of the low- and high-speed regions correspond to the downstream and upstream-pointing apexes of the zigzag strip [38]. The higher surface shear stress due to the high-speed regions agrees with the occurrence of low-temperature regions in Fig. 6f. Peaks of velocity fluctuations are produced around the bell-shaped low-speed regions, indicating the earlier start on the growth of inflectional instability compared with the grit. Further downstream, at $x/c = 0.24$ (Fig. 7f), the low-speed regions expand in both wall-normal and spanwise directions, leading to a merging between neighboring regions. The intensity of the velocity fluctuations also increases, reaching an average peak level of $0.08u_e$. At $x/c = 0.29$ (Fig. 7h), the low-speed regions are almost indistinguishable from each other, leading to a relatively uniform region with a high intensity of velocity fluctuations near the wall. A fully turbulent boundary layer is established at this station.

Increasing u_∞ to 25 m/s leads to stronger spanwise modulations above the grit at $x/c = 0.16$ (Fig. 8a). The velocity fluctuations are higher in comparison with those seen earlier for $u_\infty = 20$ m/s. Downstream of the grit at $x/c = 0.19$ (Fig. 8c), the stronger mean shear results in higher intensity of the velocity fluctuations. At $x/c = 0.24$ (Fig. 8e), the velocity fluctuations are more uniform in the spanwise direction than for the previous case, indicating a uniform onset of laminar to turbulent transition. Further downstream at $x/c = 0.29$ (Fig. 8g), high-velocity fluctuations are produced over the entire span. A fully turbulent boundary layer is obtained at this stage, which is later confirmed by the intermittency factor (Sec. V.B). The flowfield around and downstream of the zigzag strip (Fig. 8b) resembles the one for $u_\infty = 20$ m/s. The intensity of the velocity fluctuations remains similar in magnitude and in distribution at $x/c = 0.16$ and 0.19 (Figs. 8b and 8d). Downstream, at $x/c = 0.24$ (Fig. 8f), the area of low-speed regions undergoes a faster expansion, resulting in a stronger spanwise connection between neighboring regions. A more homogenous distribution of velocity fluctuations is found at $x/c =$

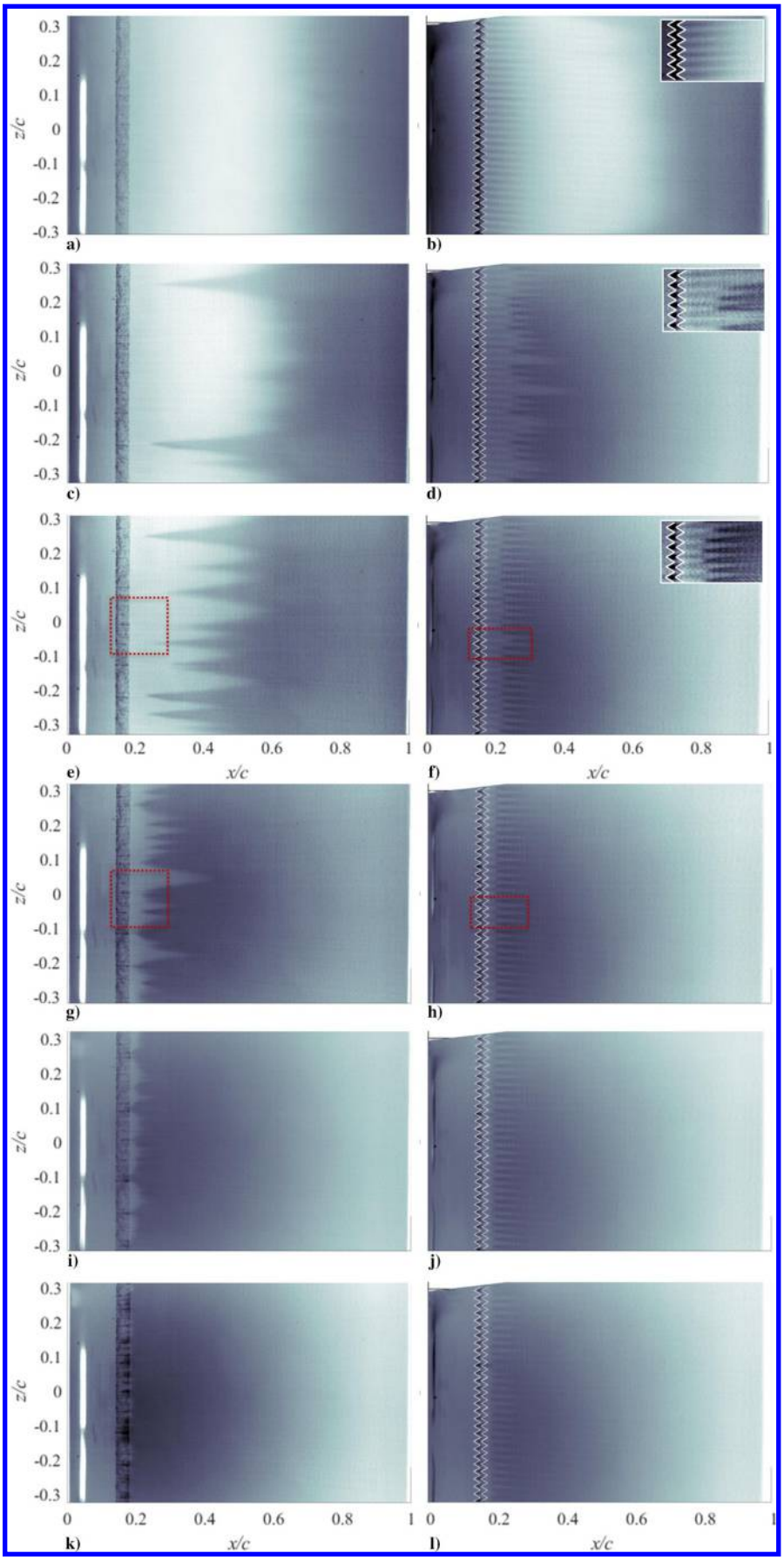

Fig. 6 Surface temperature distribution. Left and right columns correspond to grit and zigzag, respectively. The rows, from top to bottom, represent freestream velocities of $u_\infty = 16$, 18, 20, 25, 30, and 35 m/s, respectively. A zoomed in view of contours in ranges of $x/c = [0.12, 0.35]$ and $z/c = [0.12, 0.35]$ around zigzag strip are shown in top-right corners of each subfigure. Dark and light colors indicate low and high temperatures. Red boxes in Figs. 6e–6h indicate domains of hot-wire measurements.

Table 2 Transition locations behind the grit and the zigzag at different flow conditions

	u_∞, m/s					
	16	18	20	25	30	35
Grit, averaged (x_t/c)	0.70	0.57	0.42	0.24	0.20	0.15
Grit, range (x_t/c)	[0.65, 0.74]	[0.25, 0.68]	[0.23, 0.57]	[0.19, 0.39]	[0.18, 0.27]	[0.14, 0.18]
Zigzag, averaged (x_t/c)	0.68	0.28	0.23	0.20	0.20	0.19
Zigzag, range (x_t/c)	[0.61, 0.78]	[0.24, 0.40]	[0.21, 0.31]	[0.19, 0.28]	[0.19, 0.27]	[0.19, 0.25]
Undisturbed boundary layer (x_t/c)	0.84	0.83	0.80	0.77	0.74	0.71

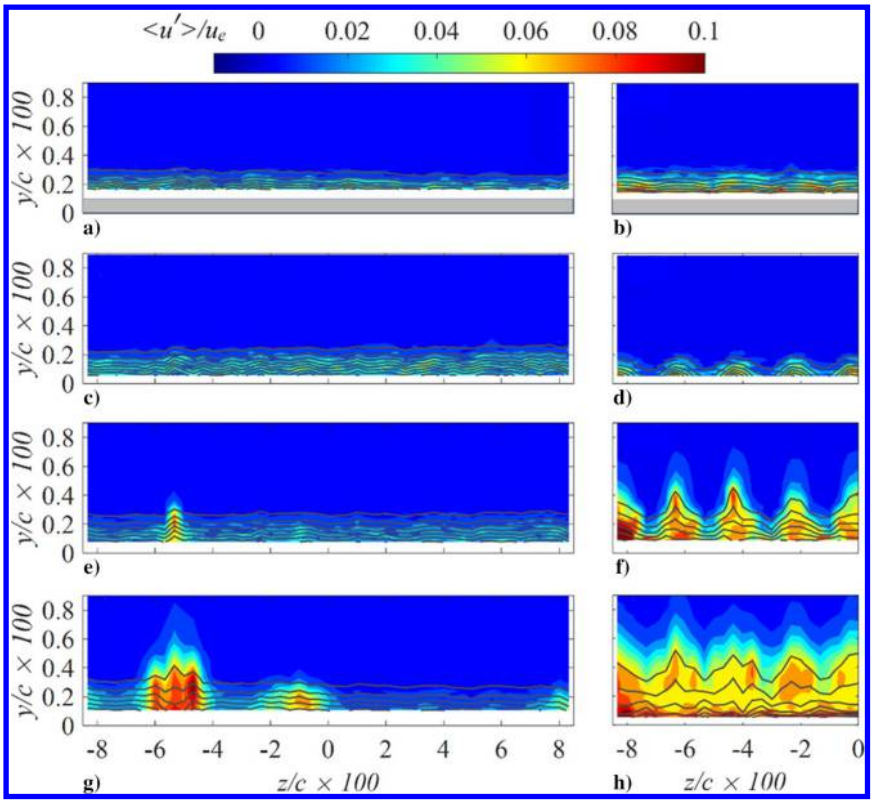

Fig. 7 Cross-plane contours of velocity fluctuations ($\langle u' \rangle / u_e$) on top and downstream of a) grit and b) zigzag at $u_\infty = 20$ m/s. Black lines represent contours of nondimensional time-averaged velocity (u/u_e) with an increment of 0.1. The rows, from top to bottom, correspond to $x/c = 0.16, 0.19, 0.24,$ and 0.29. The y axis is magnified by a factor of five for better visualization. The gray areas in Figs. 7a and 7b indicate roughness height.

0.29 (Fig. 8h), indicating a fully turbulent boundary layer at this location.

In summary, the mean boundary layer is greatly modified by the surface roughness, producing low-speed regions and three-dimensional shear layers. The localized inflectional instability leads to the growth of unstable disturbances and the onset of transition. Increasing freestream velocity from 20 to 25 m/s leads to rapid growth of velocity fluctuations for the grit and moderate growth for the zigzag, anticipating the onset of transition. Good spatial agreement has been found between the low-speed regions in Figs. 7 and 8 and the turbulent wedge shown by the surface temperature distribution in Fig. 6 (Sec. IV). The spectral content of the velocity fluctuation peaks will be elaborated on in Sec. IV.C.

B. Intermittency Detection

The stability of the low- and high-speed regions in the wake of the surface roughness is examined through the measurement of the intermittency factor γ at all of the measurement stations. The velocity fluctuation component u' is multiplied by du'/dt to detect the intermittency, following the turbulent energy recognition algorithm proposed by Zhang et al. [40]. The time signal of the velocity fluctuations over a duration of 2 s is extracted at the wall-normal location of $y = 1.1\delta^*$. The displacement thickness δ^* changes with the streamwise location. Yet, the intermittency estimate at the selected wall-normal locations is considered to be representative of the turbulent behavior in the boundary layer because γ is known to remain relatively constant in the range $y = [\delta^*, 2\delta^*]$ [41]. The time signal of the detector function corresponding to $u'du'/dt$ is averaged over a period of $\Delta t = 4$ ms. The threshold criterion is chosen by taking into account the intermittency of the undisturbed (i.e., zero roughness) laminar boundary layer. The intermittency factor γ is the fraction of the signal length when the detector ($u'du'/dt$) value is above the threshold to the total signal length. The laminar and the fully turbulent flows are represented by the γ values of zero and one, respectively. Given the limited number of measurement stations, we have chosen to associate the onset of transition with an intermittency factor of $\gamma = 0.5$ [42]. The intermittency factor is averaged across the spanwise extent of the measurement plane in order to incorporate the spanwise variation of the turbulent behavior. The results are illustrated in Fig. 9 for both the grit and zigzag cases at $u_\infty = 20$ and 25 m/s. Even though the evolution of the intermittency and the actual onset of transition cannot be fully described due to the limited measurement stations, the results provide an illustration of the establishment of a fully turbulent flow and allow a comparison with the surface temperature measurements.

Figure 9 shows that, for all test configurations, the intermittency factor is larger than zero, even at the most upstream measurement station, indicating the growth of turbulent fluctuations in close

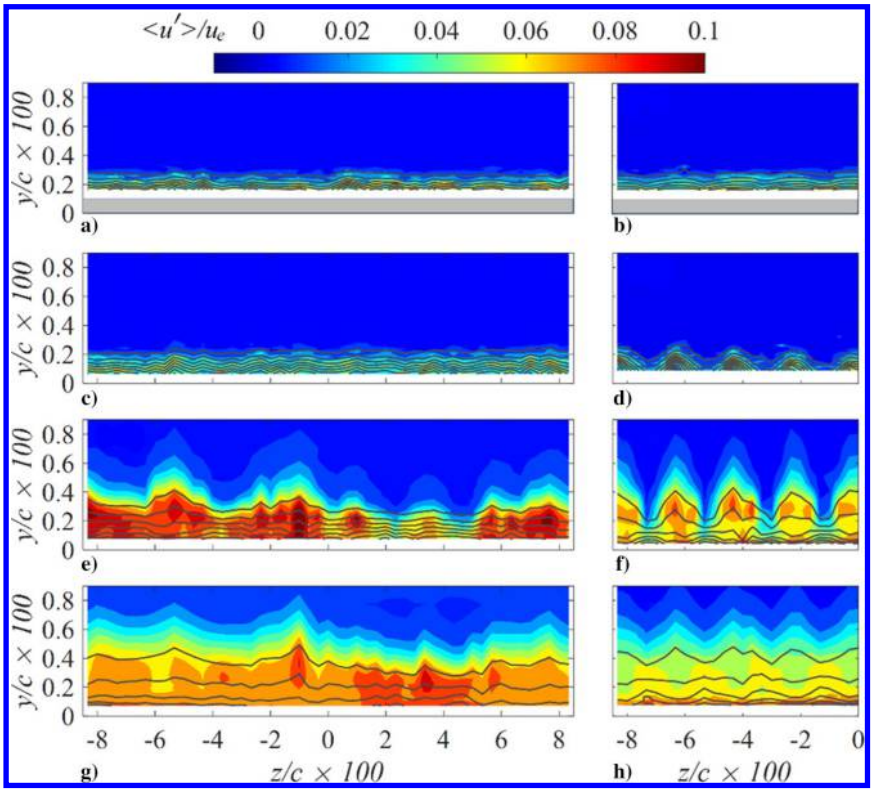

Fig. 8 Cross-plane contours of velocity fluctuations ($\langle u' \rangle / u_e$) on top and downstream of a) grit and b) zigzag at $u_\infty = 25$ m/s.

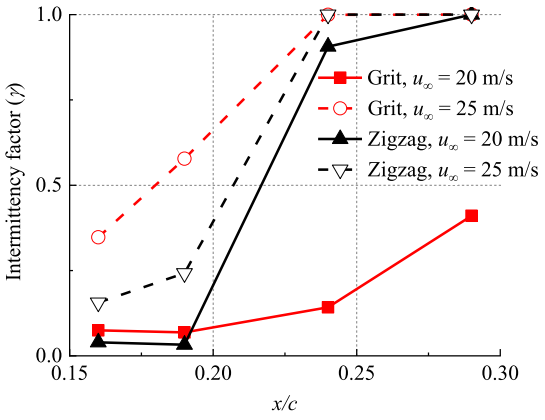

Fig. 9 Intermittency factor γ in the near wake of the grit and zigzag.

proximity of the roughness elements. For $u_\infty = 20$ m/s, the intermittency factor in the wake of the grit undergoes a mild increase and does not reach the transition threshold ($\gamma = 0.5$) at the most downstream location of $x/c = 0.29$. The zigzag is found to force an earlier onset of transition compared with the grit because the γ curve for the zigzag appears to the left of that for the grit, and furthermore reaches $\gamma = 0.5$ around $x_t/c = 0.22$. A fully turbulent boundary layer is established after $x/c = 0.29$. Both roughness configurations show good agreement with the findings from the surface temperature distribution (see Fig. 6 and Table 2).

At the higher flow speed of $u_\infty = 25$ m/s, the transition front moves rapidly upstream in the wake of the grit; and it is even closer to the roughness location with respect to the transition front behind the zigzag. The difference on the transition onset location estimated by the intermittency factor and the surface temperature measurement can be attributed to the three-dimensional shape of the turbulent wedge [17,43], which has smaller span width at the wall than that away from the wall. The surface temperature distribution provides the surface footprint of the flow structures.

For the hot-wire measurements, the mean velocity is not captured at the wall. The comparison between two measurement techniques is indirect and possibly does not lead to perfect agreement on transition location [44]. Away from the wall, the vortical structures of strong intensity introduce a high level of velocity fluctuations and earlier growth of the intermittency factor. For the zigzag trip, the evolution of the intermittency factor remains similar to the case of the lower freestream velocity, except for a slightly earlier onset of transition. A fully turbulent flow is established near $x/c = 0.24$ at the higher freestream speed.

C. Spectral Analysis

The spectral content of the transitional boundary layer is influenced by the tripping device, yielding the generation of large-scale flow structures in the wake [45–47]. To characterize the frequency of the dominant instability leading to transition in the near wake of the roughness elements, we calculate the power spectral density (PSD) of the nondimensional velocity fluctuations (u'/u_e) at the inflection points of the wall-normal shear layer within the low-speed regions for both $u_\infty = 20$ m/s and $u_\infty = 25$ m/s, as shown in Fig. 10. The streamwise location $x/c = 0.24$ is selected because of the emergence of high-level velocity fluctuations as noted in Fig. 7. The spanwise locations of low-speed regions for the grit and the zigzag correspond to $z/c = -5.33 \times 10^{-2}$ and -4.33×10^{-2}, respectively (see Figs. 7e, 7f, 8e, and 8f).

In the wake of the grit at $u_\infty = 20$ m/s (Fig. 10a), spectral peaks at 2300 Hz and its harmonics are observed for the inflection point of the low-speed region. The fundamental peak frequency corresponds to the shedding frequency of the hairpin vortices in the roughness wake [48,49]. In the wake of the zigzag strip at the same flow condition (Fig. 10a), the spectrum indicates an increase in broadband energy, in agreement with the higher level of velocity fluctuations. The vortex shedding frequency increases to 3500 Hz. Increasing the freestream velocity to $u_\infty = 25$ m/s, an increase in the broadband component of the spectrum is observed in the wake of the grit, reaching a higher level than that for the zigzag strip. No peak frequency appears in the local spectrum, indicating a fully turbulent condition. When the boundary layer is tripped by the zigzag strip, large-scale flow

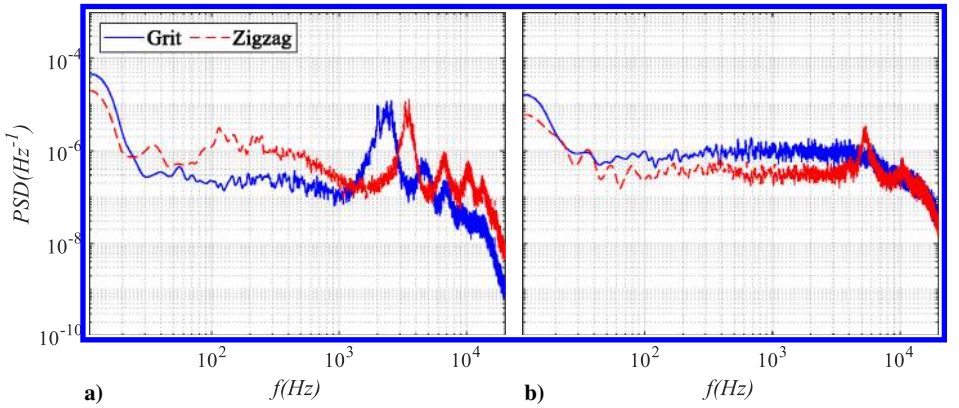

Fig. 10 Power spectral density of velocity fluctuations (u'/u_e) at $x/c = 0.24$: a) $u_\infty = 20$ m/s, and b) $u_\infty = 25$ m/s.

structures remain active in the wake of the zigzag at $u_\infty = 25$ m/s, as found in the flow topology analysis (Fig. 8b), yielding a higher vortex shedding frequency of 5300 Hz as a result of the higher value of the convective velocity.

V. Flow Properties at the Trailing Edge

The boundary layer near the trailing-edge location is characterized by the profiles of the time-averaged velocity normalized by the boundary-layer edge velocity at each measurement station (u/u_e) and the RMS of the velocity fluctuations ($\langle u' \rangle/u_e$) at $x/c = 0.95$ for $u_\infty = 20$ and 25 m/s, as shown in Fig. 11. The velocity profiles are averaged over the spanwise extent of the measurement domain. The wall-normal positions are normalized by the local boundary-layer thickness δ_{99}. The boundary-layer properties for both freestream velocities are summarized in Table 3. When the boundary layer is tripped by the grit and the zigzag strip, the velocity profiles at the trailing edge are almost identical for both cases at the same u_∞, with a peak fluctuation level of around $0.08u_e$ at $y/\delta = 0.09$. The overall shape of the velocity fluctuation profile is analogous to that of a fully turbulent boundary layer [48].

The spectral content of the turbulent fluctuations is investigated through the PSD of the velocity fluctuations (u'/u_e) at $x/c = 0.95$, $y/\delta_{99} = 0.3$, as shown Fig. 12. The Kolmogorov law for the inertial subrange spectrum [50] is compared with the measured spectra. The measured spectra follow the same decay rate as the Kolmogorov law in the frequency range of 200 to 10^4 Hz, confirming the turbulent flow condition at the trailing edge for all the flow conditions considered.

VI. Far-Field Noise

It was shown in the previous section that the boundary-layer properties near the trailing edge are very similar for both types of tripping devices. As the trailing-edge noise is closely related to the boundary-layer thickness at the trailing edge and to its spectral content, it is expected that the far-field noise characteristics would also be similar. The far-field noise, expressed in the 1/3-octave band sound pressure level L_p for the two tripping devices at six freestream velocities ($u_\infty = 16, 18, 20, 25, 30$, and 35 m/s) is plotted in Fig. 13. The L_p curves show similar trends for the grit and the zigzag. The sound pressure level grows with an increase in u_∞ as expected (i.e., according to the fifth power law). A plateau or increase of L_p is observed when $f > 3$ kHz for $u_\infty > 20$ m/s due to source non-compactness, leading to a hump in the spectra. The difference between the sound pressure level for the grit and the zigzag cases at each freestream velocity is calculated as

Table 3 Model parameters and boundary-layer properties at $x/c = 0.95$ for two selected freestream velocities[a]

	Roughness type				
	Grit	Grit	Zigzag	Zigzag	Grit, Brooks et al. [6]
c, m	0.30				0.30
b, m	0.40				0.46
R, m	1.30				1.22
Trip range (x/c)	0.14–0.18				0–0.2
Trip height, mm	0.30				0.30
u_∞, m/s	20	25	20	25	31.7
M_∞	0.059	0.073	0.059	0.073	0.093
u_τ, m/s	0.80	0.93	0.72	0.85	-
δ_{99}, mm	7.06	7.45	7.31	6.98	13.5
δ^*, mm	1.55	1.71	1.72	1.67	3.27
θ, mm	0.99	1.07	1.08	1.04	1.92
H	1.56	1.60	1.59	1.61	1.70

[a]Corresponding parameter values from the experiment of Brooks et al. [6] are shown for comparison.

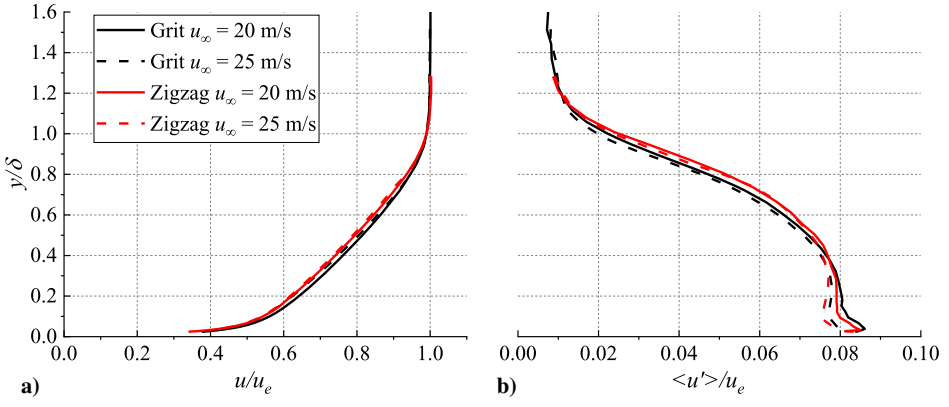

Fig. 11 Profiles of a) time-averaged velocity (u/u_e) and b) RMS of velocity fluctuations ($\langle u' \rangle/u_e$) at $x/c = 0.95$.

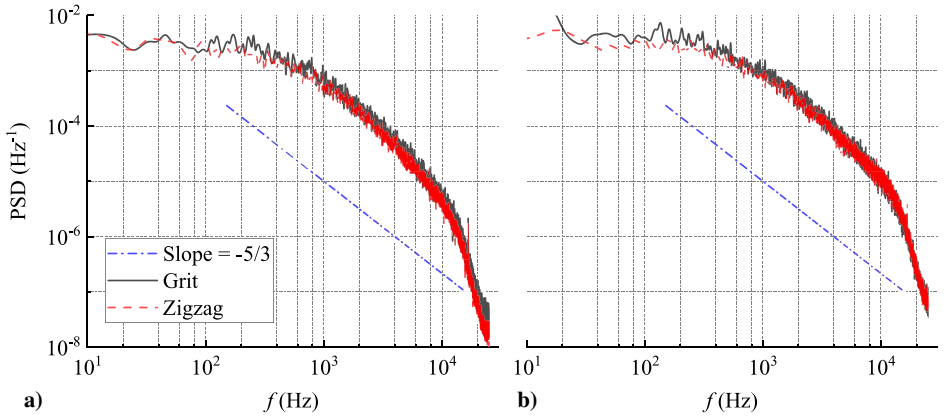

Fig. 12 Power spectral density of the velocity fluctuations at $x/c = 0.95$ and $y/\delta_{99} = 0.3$: a) $u_\infty = 20$ m/s, and b) $u_\infty = 25$ m/s.

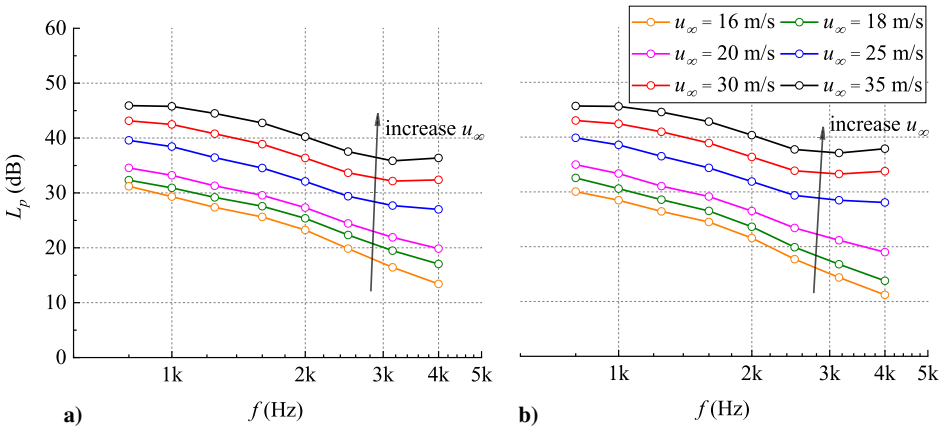

Fig. 13 Sound pressure level L_p when the boundary layer is tripped by a) the grit and b) the zigzag at different flow conditions.

$$\Delta L_p = L_{p,\text{grit}} - L_{p,\text{zigzag}} \tag{3}$$

and is plotted in Fig. 14. The value of the difference ΔL_p depends on both the freestream velocity and the frequency parameter. For $u_\infty = 16$ m/s, the grit produces a higher noise level compared with that for the zigzag strip across the entire range of frequencies measured during the experiment. The maximum ΔL_p of 2.2 dB is found at 4.0 kHz. When u_∞ is increased to 18 and 20 m/s, the noise level for the grit case is lower for $f < 1$ kHz, whereas it becomes higher at higher frequencies. Maximum noise intensity differences of 3.3 and 1.0 dB are observed at 4.0 and 2.5 kHz for $u_\infty = 18$ and 20 m/s, respectively. A further increase in u_∞ to 25 m/s causes ΔL_p to become negative, indicating that the grit produces lower noise in comparison with the zigzag strip, with a maximum ΔL_p of −1.1 dB at 4.0 kHz. A similar trend in the ΔL_p spectrum is observed at even higher u_∞ of 30 and 35 m/s, with a maximum difference at 4.0 kHz of −1.4 and −1.5 dB, respectively.

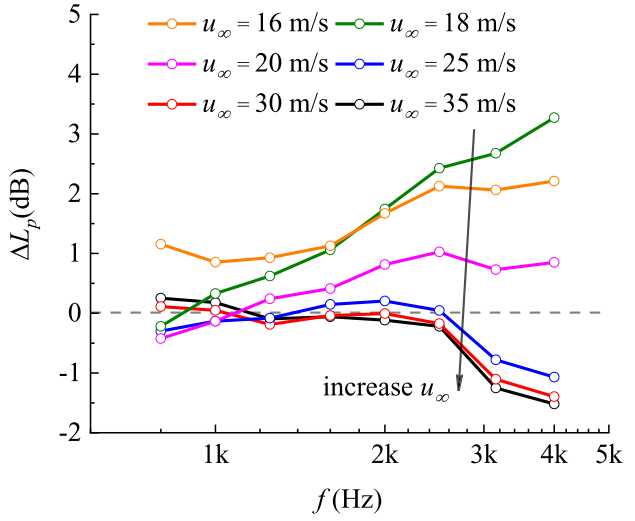

Fig. 14 Sound pressure level difference ($\Delta L_p = L_{p,\text{grit}} - L_{p,\text{zigzag}}$) between the grit and the zigzag at different flow conditions.

In summary, ΔL_p changes from a positive value to a negative value across $u_\infty = 20$ m/s. At lower u_∞, the grit is less effective in promoting boundary-layer transition. The flow remains laminar for larger streamwise extent when tripped by the grit. Large-scale vortical structures persist farther downstream in the wake, resulting in a potentially stronger spanwise correlation in the transitional regime in comparison with the correlation across the smaller-scale flow structures after the breakdown process downstream of the zigzag strip. If the higher spanwise correlation was to persist up to the trailing edge, it would lead to an increase in the noise level. When $u_\infty > 20$ m/s, the grit induces comparable or earlier onset of transition with respect to that of the zigzag. The large structures in the wake of grit undergo faster breakdown, leading to more uniform distribution of velocity fluctuations compared with the zigzag. As a result, weaker spanwise correlation of the flow structures is expected at the trailing edge for the grit, leading to a lower noise level.

The present measurements did not include spanwise correlations near the trailing edge, and hence the role of spanwise correlation cannot be established at this time. However, we note from Table 3 that the aforementioned change in the sign of ΔL_p across $u_\infty = 20$ m/s is also accompanied by a change in relative boundary-layer thickness (albeit a small one) for the grit and the zigzag strip, respectively. The transition fronts for the grit and the zigzag exhibit the largest difference at $u_\infty = 18$ m/s, leading to the highest ΔL_p. The noise level difference is more evident in the high-frequency band ($f \geq 2500$ Hz), similar to the observations of Hutcheson and Brooks [20], who

Table 4 Maximum sound pressure level difference ΔL_p and corresponding frequency f at different flow conditions

	u_∞, m/s					
	16	18	20	25	30	35
$\Delta L_{p,\max}$, dB	2.2	3.3	1.0	−1.1	−1.4	−1.5
f, kHz	4.0	4.0	2.5	4.0	4.0	4.0

applied grit and serrated tape of the same height around the leading edge. The maximum ΔL_p levels and their corresponding frequencies are summarized in Table 4.

Brooks et al. [6] measured the trailing-edge noise for the NACA 0012 airfoil. Grit particles of the same size as the current experiment were used to force transition; however, the grit was applied over a significantly larger region (from the leading edge until $0.2c$ on both upper and lower surfaces of the airfoil). The far-field noise was measured with the microphone pair. The correlation between the microphone signals accounts for the effect of the freejet shear layer of the wind tunnel and allows the subtraction of background noise. The experimental results of Brooks et al. [6] are compared with the current dataset. The latter are processed by two methods: one is the conventional beamforming algorithm (CFDBF) using the signals of the microphone array, and the other uses the signal of a single microphone located at the center of the array [center microphone (CM)]. Due to the differences between the perspective model spans, the flow conditions, and the microphone arrangements in the two experiments, the scaling of the sound pressure level with respect to the Mach number M_∞, the reference observer distance R, the model span b, and the displacement thickness δ^* at $x/c = 0.95$ [6,51] is removed via the normalized sound pressure level:

$$L_{p,\text{norm}} = L_p - 55\log(M_\infty) - 10\log(b) - 10\log(\delta^*) + 20\log(R) \quad (4)$$

The parameters for both experiments are summarized in Table 3. The normalized sound pressure level $L_{p,\text{norm}}$ is plotted against the Strouhal number St ($St = f\delta^*/u_\infty$) in Fig. 15. Instead of scaling with the fifth power of M_∞ used by Brooks et al. [6], better agreement has been found when scaling with a larger order of 5.5 [52], yielding a good collapse within 3.5 dB processed by the CFDBF for both roughness configurations employed in the present measurements at a fixed freestream speed. When using the CM, the results indicate better collapse between the noise spectra when $St > 0.15$. The exact cause for the disparity between the current data and the results of Brooks et al. remains to be determined [6]; however, it could be related to the differences between the tripping configurations. In particular, the boundary layer had been heavily tripped in the experiment by Brooks et al. [6], leading to a substantially higher boundary-layer thickness at the trailing edge in comparison with the present measurements with either type of roughness configuration. This finding indicates even a fully developed turbulent condition is reached at the trailing edge, and the measurements of airfoil trailing-edge noise remain sensitive to the details of the trip configuration.

To further validate the comparison between the present experiment and the measurements by Brooks et al. [6], the model for the wall-pressure spectrum as proposed by Kamruzzaman et al. [53] is used to estimate the far-field noise through the trailing-edge noise formulation by Roger and Moreau [54], which is available in the OptydB library (see also Ref. [55]). The aforementioned model for the wall-pressure spectrum is tuned based on NACA airfoils and incorporates the effects of the Reynolds number, boundary-layer loading, and pressure gradient. The comparison between the normalized sound pressure levels $L_{p,\text{norm}}$ obtained by the CFDBF is shown in Fig. 16.

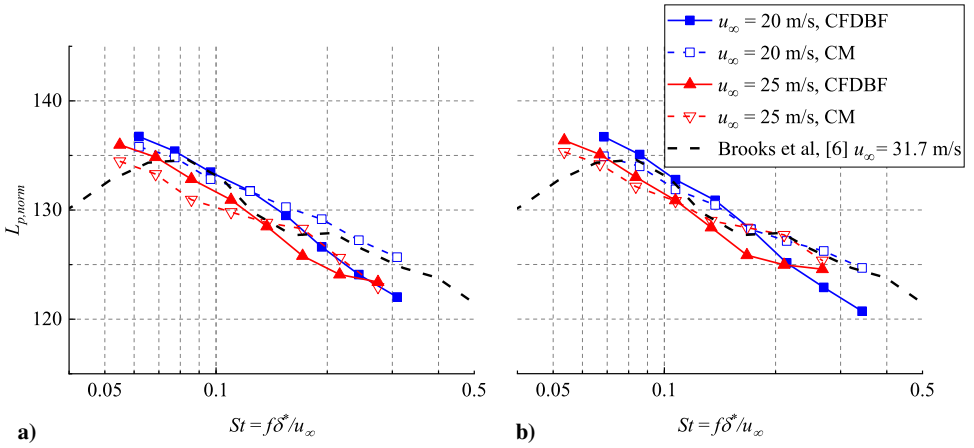

Fig. 15 Normalized sound pressure level $L_{p,\text{norm}}$ compared with work of Brooks et al. [6]: a) grit, and b) zigzag. CFDBF and CM represent results obtained by conventional beamforming and center microphone of the array, respectively.

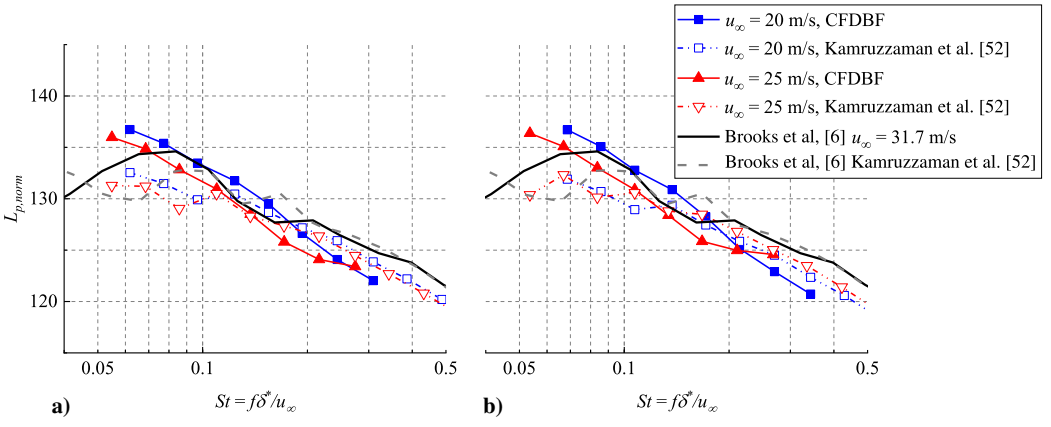

Fig. 16 Comparison of the predicted results by Kamruzzaman et al.'s model [53]: a) grit, and b) zigzag.

The predicted spectra for $L_{p,\mathrm{norm}}$ show good agreement with the experimental results when $St > 0.1$, yielding a difference of less than 3 dB. Consequently, the predicted results follow a similar trend as the experimental dataset when $St > 0.1$. For lower Strouhal numbers St, the prediction model yields larger differences in the sound pressure level, which are equal to 4 dB for the current dataset and the measurement of Brooks et al. [6]. The disparity between the predicted results also increases in the low-frequency band. Because the effect of the tripping configuration is not considered in the prediction model for the trailing-edge noise, the difference in sound pressure level may be attributed to the differences between the tripping configurations and the resulting differences in boundary-layer transition over the airfoil.

VII. Conclusions

Laminar to turbulent transition on a NACA 0012 airfoil due to randomly distributed roughness elements, as well as due to a zigzag strip, is investigated experimentally at several freestream velocities. Both roughness types with the same height are placed over the same chordwise extent of the airfoil surface, allowing the effects of both trips on the location of the transition front as well as on the far-field noise characteristics to be compared using a common experimental setup for the first time.

For randomly distributed roughness elements, low-speed regions are formed downstream of the areas where the grit is more densely distributed. High levels of velocity fluctuations are produced in these regions, leading to the onset of local turbulent wedges. For a zigzag strip, a spanwise periodic pattern of low-speed regions is generated behind the downstream-pointing apexes of the zigzag strip. The spanwise and wall-normal spreading of the low-speed regions leads to interconnection between the neighboring regions. High-intensity velocity fluctuations are produced over the entire span, leading to the onset of transition. The wake of the distributed roughness elements manifests a strong dependence on the local details of the roughness distribution, and this roughness type is found to be less effective in promoting transition than the zigzag strip at low freestream velocity ($u_\infty < 20$ m/s). When u_∞ is larger than 20 m/s, transition onset occurs across the entire span of the airfoil within a narrow range of chordwise locations, causing a rapid upstream shift of the transition front behind the distributed roughness strip and yielding the same or even a slightly upstream transition onset location in comparison with that behind the zigzag strip.

After the establishment of the fully turbulent boundary layer, however, similar boundary-layer properties are obtained near the trailing edge for both distributed roughness and the zigzag strip ($u_\infty > 20$ m/s). The far-field noise levels with different surface roughness configurations are closely related to their tripping conditions and unsteady flow features developed in the transition process. The noise level for the distributed roughness elements is higher than that of the zigzag strip at $u_\infty < 20$ m/s. At these flow conditions, large-scale vortical structures persist farther downstream in the wake of the distributed roughness elements. The strong spanwise correlation of the vortical structures in the transitional regime could be responsible for the increased noise level at these lower freestream velocities; however, this conjecture can be neither verified nor refuted due to the limitations of the present measurements. When the transition fronts behind both roughness configurations move to approximately the same chordwise locations at $u_\infty > 20$ m/s, the noise level for the distributed roughness becomes lower than that with the zigzag. The present measurements at $u_\infty = 20$ and 25 m/s achieve good agreement with the results from Brooks et al. [6]. The results reveal that an adequate characterization of both the boundary-layer properties near the trailing edge and the upstream transition process is necessary when measuring the far-field noise in wind-tunnel experiments.

Acknowledgments

The authors would like to thank Roberto Merino Martinez and Salil Luesutthiviboon for their support and suggestions on processing the acoustic data.

References

[1] Oerlemans, S., Sijtsma, P., and Méndez López, B., "Location and Quantification of Noise Sources on a Wind Turbine," *Journal of Sound and Vibration*, Vol. 299, No. 4, 2007, pp. 869–883. https://doi.org/10.1016/j.jsv.2006.07.032

[2] Zhang, X., "Airframe Noise—High Lift Device Noise," *Encyclopedia of Aerospace Engineering*, edited by R. Blockley, and W. Shyy, John Wiley & Sons, Ltd., 2010. https://doi.org/10.1002/9780470686652.eae338

[3] Moreau, S., "Turbomachinery Noise Predictions: Present and Future," *Acoustics*, Vol. 1, No. 1, 2019, pp. 92–116. https://doi.org/10.3390/acoustics1010008

[4] Moreau, S., and Roger, M., "Advanced Noise Modeling for Future Propulsion Systems," *International Journal of Aeroacoustics*, Vol. 17, Nos. 6–8, 2018, pp. 576–599. https://doi.org/10.1177/1475472X18789005

[5] Amiet, R. K., "Noise Due to Turbulent Flow Past a Trailing Edge," *Journal of Sound and Vibration*, Vol. 47, No. 3, 1976, pp. 387–393. https://doi.org/10.1016/0022-460X(76)90948-2

[6] Brooks, T. F., Pope, D. S., and Marcolini, M. A., "Airfoil Self-Noise and Prediction," NASA Rept. RP-1218, 1989.

[7] Blumer, C. B., and Van Driest, E. R., "Boundary Layer Transition-Freestream Turbulence and Pressure Gradient Effects," *AIAA Journal*, Vol. 1, No. 6, 1963, pp. 1303–1306. https://doi.org/10.2514/3.1784

[8] Wells, C. S., Jr., "Effects of Freestream Turbulence on Boundary- Layer Transition," *AIAA Journal*, Vol. 5, No. 1, 1967, pp. 172–174. https://doi.org/10.2514/3.3931

[9] Herr, M., Ewert, R., Rautmann, C., Kamruzzaman, M., Bekiropoulos, D., Arina, R., Iob, A., Batten, P., Chakravarthy, S., and Bertagnolio, F., "Broadband Trailing-Edge Noise Predictions: Overview of BANC-III Results," AIAA Paper 2015-2847, 2015.

[10] Herr, M., and Kamruzzaman, M., "Benchmarking of Trailing-Edge Noise Computations—Outcome of the BANC-II Workshop," AIAA Paper 2013-2123, 2013.

[11] Choudhari, M. M., Bahr, C., Khorrami, M. R., Lockard, D. P., Lopes, L., Zawodny, N., Herr, M., Pott-Pollenske, M., Kamruzzaman, M., Van De Ven, T., Manoha, E., Redonnet, S., Yamamoto, K., Ikeda, I., and Imamura, T., "Simulations & Measurements of Airframe Noise: A BANC Workshops Perspective," *Proceedings of the NATO STO-MP-AVT-246 Specialists Meeting on Progress and Challenges in Validation Testing for Computational Fluid Dynamics*, Avila, Spain, Sept. 2016.

[12] Klebanoff, P. S., and Tidstrom, K. D., "Mechanism by Which a Two–Dimensional Roughness Element Induces Boundary-Layer Transition," *Physics of Fluids*, Vol. 15, No. 7, 1972, pp. 1173–1188. https://doi.org/10.1063/1.1694065

[13] Saric, W. S., Reed, H. L., and Kerschen, E. J., "Boundary-Layer Receptivity to Freestream Disturbances," *Annual Review of Fluid Mechanics*, Vol. 34, No. 1, 2002, pp. 291–319. https://doi.org/10.1146/annurev.fluid.34.082701.161921

[14] Perraud, J., Arnal, D., Seraudie, A., and Tran, D., "Laminar-Turbulent Transition on Aerodynamic Surfaces with Imperfections," *RTO-AVT-111 Symposium*, Prague, Czech Republic, Oct. 2004.

[15] Fransson, J. H. M., Brandt, L., Talamelli, A., and Cossu, C., "Experimental and Theoretical Investigation of the Nonmodal Growth of Steady Streaks in a Flat Plate Boundary Layer," *Physics of Fluids*, Vol. 16, No. 10, 2004, pp. 3627–3638. https://doi.org/10.1063/1.1773493

[16] Joslin, R. D., and Grosch, C. E., "Growth Characteristics Downstream of a Shallow Bump: Computation and Experiment," *Physics of Fluids*, Vol. 7, No. 12, 1995, pp. 3042–3047. https://doi.org/10.1063/1.868680

[17] Ye, Q., Schrijer, F. F. J., and Scarano, F., "Boundary Layer Transition Mechanisms Behind a Micro-Ramp," *Journal of Fluid Mechanics*, Vol. 793, April 2016, pp. 132–161. https://doi.org/10.1017/jfm.2016.120

[18] Andersson, P., Brandt, L., Bottaro, A., and Henningson, D. S., "On the Breakdown of Boundary Layer Streaks," *Journal of Fluid Mechanics*, Vol. 428, Feb. 2001, pp. 29–60. https://doi.org/10.1017/S0022112000002421

[19] Kerho, M. F., and Bragg, M. B., "Airfoil Boundary-Layer Development and Transition with Large Leading-Edge Roughness," *AIAA Journal*, Vol. 35, No. 1, 1997, pp. 75–84. https://doi.org/10.2514/2.65

[20] Hutcheson, F. V., and Brooks, T. F., "Measurement of Trailing Edge Noise Using Directional Array and Coherent Output Power Methods," *International Journal of Aeroacoustics*, Vol. 1, No. 4, 2002, pp. 329–353. https://doi.org/10.1260/147547202765275952

[21] Cheng, B., Han, Y., Brentner, K. S., Palacios, J., Morris, P. J., Hanson, D., and Kinzel, M., "Surface Roughness Effect on Rotor Broadband Noise," *International Journal of Aeroacoustics*, Vol. 17, Nos. 4–5, 2018, pp. 438–466. https://doi.org/10.1177/1475472X18778278

[22] Sareen, A., Sapre, C. A., and Selig, M. S., "Effects of Leading Edge Erosion on Wind Turbine Blade Performance," *Wind Energy*, Vol. 17, No. 10, 2014, pp. 1531–1542. https://doi.org/10.1002/we.1649

[23] Van Rooij, R. M., and Timmer, W. A., "Roughness Sensitivity Considerations for Thick Rotor Blade Airfoils," *Journal of Solar Energy Engineering* Vol. 125, No. 4, 2003, pp. 468–478. https://doi.org/10.1115/1.1624614

[24] Winkler, J., Moreau, S., and Carolus, T., "Large-Eddy Simulation and Trailing-Edge Noise Prediction of an Airfoil with Boundary-Layer Tripping," AIAA Paper 2009-3197, 2009.

[25] Ribeiro, A. F., Casalino, D., Fares, E., and Choudhari, M., "Direct Numerical Simulation of an Airfoil with Sand Grain Roughness on the Leading Edge," NASA TM-2016-219363, 2016.

[26] Timmer, W. A., "Two-Dimensional Low-Reynolds Number Wind Tunnel Results for Airfoil NACA 0018," *Wind Engineering*, Vol. 32, No. 6, 2008, pp. 525–537. https://doi.org/10.1260/030952408787548848

[27] Hu, N., and Herr, M., "Characteristics of Wall Pressure Fluctuations for a Flat Plate Turbulent Boundary Layer with Pressure Gradients," AIAA Paper 2016-2749, 2016.

[28] Drela, M., "XFOIL: An Analysis and Design System for Low Reynolds Number Airfoils," *Low Reynolds Number Aerodynamics: Proceedings of the Conference Notre Dame*, Springer, Berlin, Heidelberg, June 1989, pp. 1–12.

[29] Tropea, C., and Yarin, A. L., *Springer Handbook of Experimental Fluid Mechanics*, Springer Science and Business Media, New York, 2007, pp. 1399–1417.

[30] Luesutthiviboon, S., Malgoezar, A., Snellen, M., Sijtsma, P., and Simons, D., "Improving Source Discrimination Performance by Using an Optimized Acoustic Array and Adaptive High-Resolution Clean-Sc Beamforming," *7th Berlin Beamforming Conference*, Berlin, Germany, March 2018.

[31] Underbrink, J. R., "Circularly Symmetric, Zero Redundancy, Planar Array Having Broad Frequency Range Applications," U.S. Patent No. 6,205,224, 2001.

[32] Merino-Martínez, R., Luesutthiviboon, S., Zamponi, R., Carpio, A. R., Ragni, D., Sijtsma, P., Snellen, M., and Schram, C., "Assessment of the Accuracy of Microphone Array Methods for Aeroacoustic Measurements," *Journal of Sound and Vibration*, Vol. 470, March 2020, Paper 115176. https://doi.org/10.1016/j.jsv.2020.115176

[33] Brandt, A., *Noise and Vibration Analysis: Signal Analysis and Experimental Procedures*, John Wiley & Sons, United Kingdom, 2011.

[34] Merino Martinez, R., Sijtsma, P., and Snellen, M., "Inverse Integration Method for Distributed Sound Sources," *7th Berlin Beamforming Conference*, Berlin, Germany, March 2018.

[35] Rayleigh, L. F. R. S., "Investigations in Optics, with Special Reference to the Spectroscope," London, Edinburgh, and Dublin *Philosophical Magazine and Journal of Science*, Series 5, Vol. 8, No. 49, 1879, pp. 261–274. https://doi.org/10.1080/14786447908639684

[36] Sarradj, E., Herold, G., Sijtsma, P., Martinez, R. M., Geyer, T. F., Bahr, C. J., Porteous, R., Moreau, D., and Doolan, C. J., "A Microphone Array Method Benchmarking Exercise Using Synthesized Input Data," AIAA Paper 2017-3719, 2017.

[37] Rubio Carpio, A., Merino Martínez, R., Avallone, F., Ragni, D., Snellen, M., and Van Der Zwaag, S., "Experimental Characterization of the Turbulent Boundary Layer over a Porous Trailing Edge for Noise Abatement," *Journal of Sound and Vibration*, Vol. 443, March 2019, pp. 537–558. https://doi.org/10.1016/j.jsv.2018.12.010

[38] Elsinga, G. E., and Westerweel, J., "Tomographic-PIV Measurement of the Flow Around a Zigzag Boundary Layer Trip," *Experiments in Fluids*, Vol. 52, No. 4, 2012, pp. 865–876. https://doi.org/10.1007/s00348-011-1153-8

[39] Ye, Q., Schrijer, F. F. J., and Scarano, F., "On Reynolds Number Dependence of Micro-Ramp-Induced Transition," *Journal of Fluid Mechanics*, Vol. 837, Feb. 2018, pp. 597–626. https://doi.org/10.1017/jfm.2017.840

[40] Zhang, D. H., Chew, Y. T., and Winoto, S. H., "Investigation of Intermittency Measurement Methods for Transitional Boundary Layer Flows," *Experimental Thermal and Fluid Science*, Vol. 12, No. 4, 1996, pp. 433–443. https://doi.org/10.1016/0894-1777(95)00133-6

[41] Matsubara, M., Alfredsson, P. H., and Westin, K. J. A., "Boundary Layer Transition at High Levels of Free Stream Turbulence," *ASME 1998 International Gas Turbine and Aeroengine Congress and Exhibition*, Vol. 1: Turbomachinery, Stockholm, Sweden, June 1998. https://doi.org/10.1115/98-GT-248

[42] Schlichting, H., and Krause, E., *Boundary Layer Theory*, Springer-Verlag, Berlin, 2003, pp. 497–517.

[43] Zhong, S., Chong, T. P., and Hodson, H. P., "A Comparison of Spreading Angles of Turbulent Wedges in Velocity and Thermal Boundary Layers," *Journal of Fluids Engineering*, Vol. 125, No. 2, 2003, pp. 267–274. https://doi.org/10.1115/1.1539871

[44] Avallone, F., Schrijer, F. F. J., and Cardone, G., "Infrared Thermography of Transition due to Isolated Roughness Elements in Hypersonic Flows," *Physics of Fluids*, Vol. 28, No. 2, 2016, Paper 024106. https://doi.org/10.1063/1.4941527

[45] Ye, Q., Schrijer, F. F. J., and Scarano, F., "Geometry Effect of Isolated Roughness on Boundary Layer Transition Investigated by Tomographic PIV," *International Journal of Heat and Fluid Flow*, Vol. 61, Oct. 2016, pp. 31–44. https://doi.org/10.1016/j.ijheatfluidflow.2016.05.016

[46] Iyer, P. S., and Mahesh, K., "High-Speed Boundary-Layer Transition Induced by a Discrete Roughness Element," *Journal of Fluid Mechanics*, Vol. 729, Aug. 2013, pp. 524–562. https://doi.org/10.1017/jfm.2013.311

[47] Muppidi, S., and Mahesh, K., "Direct Numerical Simulations of Roughness-Induced Transition in Supersonic Boundary Layers," *Journal of Fluid Mechanics*, Vol. 693, No. 2, 2012, pp. 28–56. https://doi.org/10.1017/jfm.2011.417

[48] Klebanoff, P. S., Cleveland, W. G., and Tidstrom, K. D., "On the Evolution of a Turbulent Boundary Layer Induced by a Three-Dimensional Roughness Element," *Journal of Fluid Mechanics*, Vol. 237, April 1992, pp. 101–187. https://doi.org/10.1017/S0022112092003379

[49] Acarlar, M. S., and Smith, C. R., "A Study of Hairpin Vortices in a Laminar Boundary Layer. Part 1. Hairpin Vortices Generated by a Hemisphere Protuberance," *Journal of Fluid Mechanics*, Vol. 175, Feb. 1987, pp. 1–41. https://doi.org/10.1017/S0022112087000272

[50] Kolmogorov, A. N., Levin, V., Hunt, J. C. R., Phillips, O. M., and Williams, D., "The Local Structure of Turbulence in Incompressible Viscous Fluid for Very Large Reynolds Numbers," *Proceedings of the Royal Society of London, Series A: Mathematical and Physical Sciences*, Vol. 434, No. 1890, 1991, pp. 9–13. https://doi.org/10.1098/rspa.1991.0075

[51] Avallone, F., Van Der Velden, W. C. P., Ragni, D., and Casalino, D., "Noise Reduction Mechanisms of Sawtooth and Combed-Sawtooth Trailing-Edge Serrations," *Journal of Fluid Mechanics*, Vol. 848, Aug. 2018, pp. 560–591. https://doi.org/10.1017/jfm.2018.377

[52] Carpio, A. R., Avallone, F., Ragni, D., Snellen, M., and Zwaag, S. V. D., "3D-Printed Perforated Trailing Edges for Broadband Noise Abatement," *25th AIAA/CEAS Aeroacoustics Conference*, AIAA Paper 2019-2458, 2019.

[53] Kamruzzaman, M., Bekiropoulos, D., Lutz, T., Würz, W., and Krämer, E., "A Semi-Empirical Surface Pressure Spectrum Model for Airfoil Trailing-Edge Noise Prediction," *International Journal of Aeroacoustics*, Vol. 14, Nos. 5–6, 2015, pp. 833–882. https://doi.org/10.1260/1475-472X.14.5-6.833

[54] Roger, M., and Moreau, S., "Back-Scattering Correction and Further Extensions of Amiet's Trailing-Edge Noise Model. Part 1: Theory," *Journal of Sound and Vibration*, Vol. 286, No. 3, 2005, pp. 477–506. https://doi.org/10.1016/j.jsv.2004.10.054

[55] Romani, G., Van der Velden, W. C., and Casalino, D., "Deterministic and Statistical Analysis of Trailing-Edge Noise Mechanisms with and Without Serrations," AIAA Paper 2018-3129, 2018.

D. Zhao
Associate Editor